Carbon 201 (2023) 189–199

Contents lists available at ScienceDirect

Carbon

journal homepage: www.elsevier.com/locate/carbon

Research paper

Atomic insights into mechanisms of carbon coating on titania nanoparticle during flame synthesis

Dingyu Hou [a], Qian Mao [b], Yihua Ren [c,*], Kai H. Luo [a,*]

[a] Department of Mechanical Engineering, University College London, Torrington Place, London, WC1E 7JE, UK
[b] Institute of Technology for Nanostructures, University Duisburg–Essen, Duisburg, 47057, Germany
[c] Institute for Combustion Technology, RWTH Aachen University, Templergraben 64, Aachen, 52056, Germany

ARTICLE INFO

Keywords:
Carbon coating
ReaxFF
Reactive molecular dynamics simulation
Titania nanoparticle
Hydrocarbons inception

ABSTRACT

Carbon-metal oxide (CMO) nanocomposites have seen increasing research due to their extraordinary properties for energy storage materials and photocatalysts. Flame aerosol synthesis provides a promising route to producing CMO nanocomposites. Various CMO nanocomposites have been successfully synthesized through flame aerosol techniques in laboratories. However, a detailed understanding of the formation and growth mechanisms of such materials is lacking. Therefore, in this study, the reactive force-field molecular dynamics (ReaxFF MD) was deployed to gain atomic insights into the initial stage of carbon coating on the titania nanoparticle. We performed a large number of simulations of carbon coating with 18 typical hydrocarbon species in flames including aliphatics of C1–C4 species and polycyclic aromatic hydrocarbons (PAHs) at temperatures ranging from 400 K to 2500 K. We found that the titania nanoparticle can not only serve as a nucleus for physical adsorption of the surrounding hydrocarbons, but also can form C–Ti/O bonds with them, and abstract H atoms from the surrounding hydrocarbons. The optimal temperature range for carbon coating is $T \leq 1200$ K, because C–Ti/O bonds are unstable at higher temperatures. At $T \geq 1500$ K, hydrocarbons tend to gather to form larger carbonaceous species instead of coating onto the particle surface, as the formation of C–C bonds is promoted at high temperatures. Small aliphatics are favored to be chemically coated on the particle, while PAH molecules tend to be physically absorbed on the nanoparticle surface due to their stable electronic structure and large size. Coating tendencies of aliphatics are closely related to the number of C–C triple bonds.

1. Introduction

Carbon-metal oxide (CMO) nanocomposites have drawn increasing attention of researchers and industries due to their extraordinary properties for energy storage materials and photocatalysts [1]. As one of the most important energy storage techniques, the lithium-ion battery (LIB) has seen intense research efforts in recent years aimed at better electrochemical performance, higher stability and lower cost [2]. For example, although LIB with $LiCoO_2$ (LCO) cathode and graphite anode has been commercialized in 1991, attempts to find more cost-effectively and environmental-friendly electrode materials have never ceased [2]. Transition metal oxides such as MnO_x, CoO_x, NiO_x, FeO_x, etc., appear to be promising anode materials for LIB due to their high lithium storage capacity, low cost and low toxicity [3,4]. However, large volume change of the transition metal oxides during the Li-ion insertion/extraction process results in electrode pulverization and rapid capacity fade, which significantly impedes their practical applications [5–7]. As for alternative cathode materials, $LiFePO_4$ is of great potential because it is cheap and environmentally benign, and shows a high cycle stability as well [8,9]. Nonetheless, the low electric conductivity of $LiFePO_4$ limits its application. Fortunately, previous studies have suggested that the aforementioned limitations of the two electrode materials can be effectively addressed by coating a layer of carbon materials, due to the good electronic conductivity of the carbon layer [10–13]. In addition, the coated layer can also buffer the volume change during Li-ion insertion/extraction. Besides electrode materials, carbon coating of the photocatalyst anatase type TiO_2 has been found to give many advantages including stable crystal phase, high photocatalytic activity under visible light irradiation, and strong adsorptivity. Therefore, carbon-coated TiO_2 can be applied to oxidize different organic contaminants in water [14,15]. Other practical usages of carbon-coated TiO_2 includes precursors for TiC, gray pigments, etc [16–19].

* Corresponding authors.
E-mail addresses: y.ren@itv.rwth-aachen.de (Y. Ren), k.luo@ucl.ac.uk (K.H. Luo).

https://doi.org/10.1016/j.carbon.2022.09.002
Received 20 May 2022; Received in revised form 7 August 2022; Accepted 1 September 2022
Available online 5 September 2022

Typically, CMO products are produced by separate synthesis of the metal oxide and carbon particles followed by cumbersome powder mixing [1,19]. In contrast, gas-phase synthesis route like flame aerosol synthesis offers an alternative bottom-up route for these products in a single-step, continuous, and scalable way, which prevails over the wet chemistry and solid processing approaches [19–22]. This approach has been commercialized in simple nanomaterials like carbon black, titania (TiO_2), and silica (SiO_2) [23,24], and is now innovating towards synthesizing complex nanocomposites. So far various CMO nanocomposites such as C-coating SiO_2 [25], C-coating TiO_2 [19,26], and C-coating $LiFePO_4$ nanoparticles [11] have been successfully synthesized using flame aerosol technology in laboratories. These pioneering studies have shown that the fuel-oxidant equivalence ratio and metal precursor concentration can affect the morphology of the synthesized CMO, thus making it possible to actively control the core size of metal oxides and the carbonaceous layer thickness by adjusting certain flame parameters [11,19,26,27]. This is of vital importance in optimizing the performance of carbon-coated nanoparticles for different application scenarios via changing/controlling the layer thickness, and/or the crystal phase of the metal oxides [13,15,28]. To enable tailoring the morphology of the gas-phase-synthesized CMO particles, a better understanding towards the detailed formation and growth mechanisms of CMO is required. Kammler and Pratsinis [19] conducted a pioneering study on the concurrent synthesis of titania-carbon nanoparticles using a diffusion flame aerosol reactor for combustion of titanium tetraisopropoxide (TTIP, $Ti(OC_3H_7)_4$) and acetylene (C_2H_2). Graphitic layered carbon-coated titania particles, pure carbon particles, and non-coated titania particles were observed at various fuel flow rates. Waser et al. [11] achieved continuous flame synthesis of core–shell $LiFePO_4$-carbon nanoparticles in an enclosed flame spray pyrolysis reactor. By changing the fuel-oxidant equivalence ratio, different product morphology, i.e., the $LiFePO_4$-C core–shell structure and segregated $LiFePO_4$ and acetylene carbon black particles were obtained. More recently, Ren et al. [26] investigated the formation mechanism of the core–shell titania-carbon nanocomposites in a well-defined counterflow burner using an in-situ laser diagnostic method and transmission electron microscopy (TEM) of synthesized nanocomposites. Their experimental results show that the synthesis of CMO nanocomposites includes two sequential stages: (1) the metal oxides form and grow in the oxidizer side of the diffusion flame sheet; (2) the nanoparticles are coated with carbonaceous species in the fuel-rich zone. Based on the understanding, independent active control of the core size and coating layer thickness was then achieved. However, in these previous experimental studies, a convincing model describing the coating process is lacking. It is unclear whether the metal oxide nanoparticles serve solely as nuclei for physical condensation of carbonaceous species or they can also form chemical bonds with the adsorbed carbonaceous species.

Since the onset of the carbon coating process in flames can be extremely fast, it is difficult to investigate the initial coating process based merely on experimental instruments. The frequently used transmission electron microscopy (TEM) technique is helpful in revealing the morphology of the flame synthesized CMO nanocomposites [11,19,25–27]. However, this ex-situ technique is unable to capture the dynamic process of how carbonaceous materials are coated on metal oxide nanoparticles in flames. In principle, the in-situ laser diagnostic method can be applied to measure the growth process of CMO nanocomposites in flames, but in reality, it is very challenging to quantify particle properties such as volume fraction using the laser-induced incandescence (LII) signal [26,29]. Crucially, the physical and chemical mechanisms of coating of the carbonaceous species onto metal oxide particles are hard to separate through experimental observations. As complements to current experimental techniques, some state-of-the-art simulation approaches may be employed to explore the carbon coating process in flames and provide atomic insights. The reactive force-field molecular dynamics (ReaxFF MD) serves as a bridge between quantum mechanics (QM) and classical non-reactive MD [30]. ReaxFF MD has QM's capability for simulating bond breaking and forming, thus chemical reactions, while it has an affordable computational cost comparable to that of the classical MD. It allows for simulation of the dynamic evolution of a system of $\sim 10^4$ atoms for tens of nanoseconds involving chemical reactions in routine studies. Ab initio molecular dynamics (AIMD) can also simulate chemical reactions with good accuracy in computing potential energy surfaces. However, the high computational cost of AIMD restricts routine simulations to $\sim 10^2$ atoms and $\sim 10^{-2}$ – 10^{-1} nanoseconds [31,32], which is insufficient to capture the carbon coating process in terms of system sizes and time scales. Therefore, ReaxFF MD as a powerful computational tool has already been extensively applied to simulate a variety of physicochemical processes in flames [33–37]. For instance, we have previously elucidated the inception mechanism of TTIP precursor converting to Ti-containing clusters in the context of flame-synthesized nanomaterials using ReaxFF MD simulations [37]. Regarding the carbon coating process, Hong and van Duin [38] developed a ReaxFF force field for Al/C interactions, based on which the mechanism of different carbonaceous precursors coating on aluminum nanoparticles was studied. However, to the best of the authors' knowledge, the detailed mechanism of carbonaceous species coating on metal oxide nanoparticles has not been reported in the literature. Therefore, in this work, we investigate the interaction mechanism of hydrocarbon species with a titania nanoparticle using ReaxFF MD simulations in the context of flame-synthesized functional nanomaterials. Meanwhile, the coating tendencies of various hydrocarbons on a titania nanoparticle are compared and the optimal temperature range of carbon coating is identified.

2. Simulation methods

2.1. Ti/C/H/O ReaxFF force field

ReaxFF is a general bond-order-dependent force field that enables the description of bond dissociation and bond formation. In ReaxFF MD simulations, bond orders are directly calculated between all pairs of atoms from their interatomic distances at every iteration, making a smooth transition between the non-bonded states and single, double or triple bonded states possible, leading to the simulation of chemical reactions properly. The total energy in ReaxFF is described by the following energy terms:

$$E_{system} = E_{bond} + E_{lp} + E_{over} + E_{under} + E_{val} + E_{pen} + E_{coa} + E_{C2} + E_{triple} + E_{tors} + E_{conj} + E_{Hbond} + E_{vdWaals} + E_{Coulomb} \quad (1)$$

The energy of the system (E_{system}) includes both bonded and non-bonded interactions. Bonded interactions are bond-order dependent, including the bond energy (E_{bond}), lone pair energy (E_{lp}), over-coordination energy (E_{over}), under coordination energy (E_{under}), valence-angle energy (E_{val}), penalty energy (E_{pen}), three-body conjugation energy (E_{coa}), torsion-angle energy (E_{tors}), four-body conjugation energy (E_{conj}), hydrogen bond energy (E_{Hbond}), C2 energy correction (E_{C2}), and triple bond energy correction (E_{triple}). Non-bonded interactions including van der Waals energy ($E_{vdWaals}$) and Coulomb energy ($E_{Coulomb}$) are calculated between each pair of atoms in the system. Besides E_{bond}, E_{over}, E_{angle}, E_{tors}, $E_{vdWaals}$, and $E_{Coulomb}$, other terms in Eq. (1) are system specific — they will be included only when they are necessary to capture properties particular to the system of interest [30]. Atomic charges are derived from an electronegativity equalization method (EEM) [39] with a shielding term to prevent excessive short-range interactions. Details about the full function forms of the ReaxFF method can be found in Refs. [30,40,41]. In this work, we used the parameters of the Ti/C/H/O ReaxFF force field provided in Ref. [42] to perform reactive MD simulations. This Ti/C/H/O ReaxFF is developed by enriching the training set of the well-trained Ti/O/H interactions [43,44] with additional density functional theory (DFT) data on Ti-C bond dissociations, C–Ti-C/O angle descriptions, and the energy of condensed phases [45,46]. The original Ti/O/H force field

has been shown to successfully describe the interaction of water with different oriented TiO_2 surfaces [43,47,48]. By introducing interaction between C and Ti/O/H, the newly developed Ti/C/H/O force field has been widely used to investigate systems related to MXene materials ($Ti_3C_2T_x$, T_x: -O, -OH, and/or -F) in various situations, including solutions [42,45,46,49], surface reactions [50], thermal decomposition and oxidation [51,52], as well as derivations for some fundamental mechanical properties [53,54]. These successful implementations of the Ti/C/O/H force field in previous ReaxFF MD studies demonstrate its capability of describing systems governed by Ti/C/O/H interactions in a broad temperature range from room temperature to 3000 K. Therefore, we employed this Ti/C/O/H ReaxFF to simulate the process of carbon coating on TiO_2 nanoparticles in the context of flame aerosol synthesis, aiming at providing atomic insights into the growth mechanism of carbonaceous materials on TiO_2 nanoparticle surface.

2.2. Simulation setup

The prototype of the ReaxFF MD simulations in present work comes from our recent experimental study [26], in which carbon coated titania nanoparticles were synthesized in a well-defined counter-flow burner, with ethylene (C_2H_4) being the fuel as well as the carbon source for coating, and titanium tetraisopropoxide (TTIP, $Ti(C_3H_7O)_4$) being the precursor for titania nanoparticles. Figure 1(a) illustrates the initial configuration for simulating hydrocarbon species coating on a titania nanoparticle. The size of the simulation box is $100 \times 100 \times 100$ Å^3. The diameter of the titania nanoparticle is around 3 nm and is placed at the center of the simulation box. The initial configuration of the surrounding hydrocarbon species is generated by randomly packing n C_mH_n molecules/radicals in the region outside the nanoparticle and inside the simulation box using the PACKMOL software [55]. To generate the initial atom coordinates of the titania nanoparticle, we first cut out a 3 nm spherical nanoparticle from the bulk anatase material, and then performed equilibration on this structure at $T = 1800$ K for > 2 ns. We chose 1800 K because it is the maximum temperature on the oxidizer side of the counterflow flame in Ren et al. [26]'s experiments when they synthesized carbon-coated TiO_2 nanoparticles, and TiO_2 nanoparticles were generated in the oxidizer side of the counterflow flame with titanium tetraisopropoxide (TTIP) being the precursor. Three structures after 2 ns equilibration at 1800 K have been selected as the initial configurations (configurations at 2000, 2010, and 2020 ps) for C coating simulation. Note that at 1800 K, a small number of O_2 molecules were released from the titania nanoparticle during the equilibration, leading to an O/Ti ratio ($Ti_{420}O_{728}$) smaller than 2. The desorption of O_2 is caused by the lower chemical potential of oxygen in the gas phase than that in the metal oxide phase. The desorption of O_2 in an oxygen-deficient condition is not only a natural process but also in accordance with experimental conditions [56–58]. In order to investigate the effect of different O/Ti ratios of the titania nanoparticle on carbon coating, we also equilibrated the 3 nm titania nanoparticle at two lower temperatures – 1200 K and 1500 K for 2 ns after it is cut out from the bulk anatase material, so as to obtain titania nanoparticles with different O/Ti ratios. Higher temperature can promote O_2 desorption, hence resulting in titania nanoparticles with lower O/Ti ratios. $Ti_{420}O_{814}$ was obtained after equilibration at 1200 K and $Ti_{420}O_{776}$ at 1500 K. Then 600 C_4H_2 molecules were simulated to coat on three titania nanoparticles with different O/Ti ratios at 800 K. Results show that the initial O/Ti ratio has a slight influence on the chemisorption of hydrocarbons on the titania nanoparticle surface, while its influence on the physical adsorption can be ignored. More detailed results and discussion can be found in the Supporting Information (SI).

Selection of the hydrocarbon species surrounding the titania nanoparticle to perform the carbon coating simulation is not trivial. Based on existing experimental studies, it is only aware that hydrocarbon fuels are the source of carbon element when carbon-coated metal oxide nanoparticles are synthesized through flame reactors [11,19,26]. However, numerous intermediate species C_mH_n can be involved in the pyrolysis of hydrocarbon fuels, and it is highly likely that they exhibit different propensities upon coating on the surface of a metal oxide nanoparticle. Appreciable efforts have been made by experimentalists in detecting and identifying key intermediates species in flames [59], facilitated by a series of advanced experimental instruments such as gas chromatography/mass spectrometry (GC/MS) [60,61] and laser-induced fluorescence (LIF) [62]. As one of the most studied fuels in the combustion community, C_2H_4 flames have a great deal of experimental data on chemical speciation obtained from different burner configurations under various temperature and pressure conditions. In such flames, small hydrocarbon species including methane (CH_4), acetylene (C_2H_2), C_2H_4, propargyl (C_3H_3), diacetylene (C_4H_2), vinylacetylene (C_4H_4), 1,3-butadiene (C_4H_6) are generally reported as major intermediate species [60,61,63]. In addition to experimental data, we also carried out ReaxFF MD simulations on pyrolysis of C_2H_4 to identify the key intermediate species from the modeling point of view. Details of the C_2H_4 pyrolysis simulation can be found in SI, where the temporal evolution of the number of C1–C4 molecules/radicals during the pyrolysis simulation is plotted in Fig. S3. On the basis of the available experimental data and MD simulation results on C_2H_4 pyrolysis, we selected 12 typical C1–C4 small hydrocarbon species to investigate their coating behaviors on a titania nanoparticle, as shown in Cases 1, 2, 3, and 4 in Fig. 1(a). Besides aliphatic species, polycyclic aromatic hydrocarbons (PAHs) also play an important role as key intermediates during pyrolysis and fuel-rich combustion of hydrocarbon fuels, because they are generally believed to be the major precursors of soot [64]. Therefore, Cases 5(a), 5(b), 6, 7(a), 7(b), and 8 are designed to examine the coating properties of six PAH molecules/radicals from one aromatic ring (benzene (C_6H_6)) to ten aromatic rings (ovalene ($C_{32}H_{14}$)), in accordance with the common size range for aromatic species reported by experimental measurements [65]. Molecular structures of the aliphatic species containing four carbon atoms (C4 species) and the aromatic species are provided in Fig. 1(c). In order to make comparison of the tendency of coating on the titania nanoparticle among different hydrocarbon species, the total number of C atoms in the surrounding hydrocarbons is kept the same, i.e., 2400, in all ten cases. To explore the effect of temperature, for each of the ten cases, we performed carbon coating simulations at seven different temperatures, namely 400 K, 800 K, 1200 K, 1500 K, 1800 K, 2000 K, and 2500 K, which cover the temperature range in common flame aerosol synthesis.

ReaxFF MD simulations in this work are performed using the Large-scale Atomic/Molecular Massively Parallel Simulator (LAMMPS) package [66] implemented with reax/c [41,67]. For each case, we start the simulation with potential energy minimization using the conjugated gradient (CG) algorithm to eliminate possible irrational initial geometries, which may be induced by assembling the titania nanoparticle with the surrounding C_mH_n species. Then the canonical ensemble (NVT) is employed to simulate the carbon coating process. Nosé–Hoover thermostat with a damping constant 10 fs is used to control the system temperature at the desired value. The total simulation time of carbon coating lasts for 2 ns with a 0.1 fs time step. Snapshots are prepared by Visual Molecular Dynamics (VMD) software [68] and OVITO [69]. To indicate the statistical noise of the MD simulation results, three replica simulations with different initial configurations for some of the typical cases at various temperatures were performed, including Cases 1, 2, 3, 4, and 6 at 800 K; Case 7b at 1200 K; Case 4 at 2000 K; Case 7a at 2500 K. The initial configurations for these replica simulations are built by assembling the three titania nanoparticles of different initial configurations with surrounding hydrocarbons at different initial positions. For other simulation conditions, we generated one trajectory instead of three to reduce the huge computational cost (e.g., the performance of 600 C4 species coating on a 3 nm titania nanoparticle at 2000 K is 0.492 ns/day on 128 cores). Detailed simulation results of the three replica runs, together with the averaged results and the standard deviations have been listed in Tables S1, S2, S3, S4, and S5 in the Supporting Information (SI).

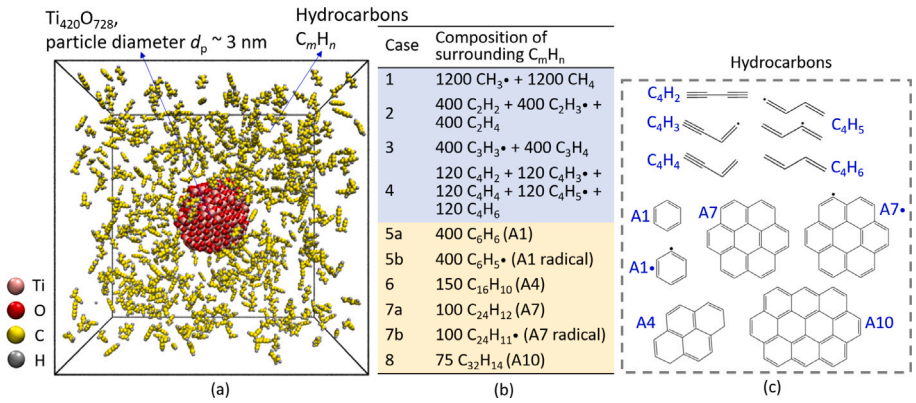

Fig. 1. Illustration of the initial simulation configuration for carbon coating on a 3 nm titania nanoparticle (a); Composition of surrounding C_mH_n species for different simulation cases. Light blue region denotes short-chain aliphatic species, while light yellow region denotes polycyclic aromatic hydrocarbon (PAH) species. The black dot indicates the species is a radical (b); Molecular structure for C_4H_2, C_4H_3, C_4H_4, C_4H_5, C_4H_6 and PAH species (c). (For interpretation of the references to color in this figure legend, the reader is referred to the web version of this article.)

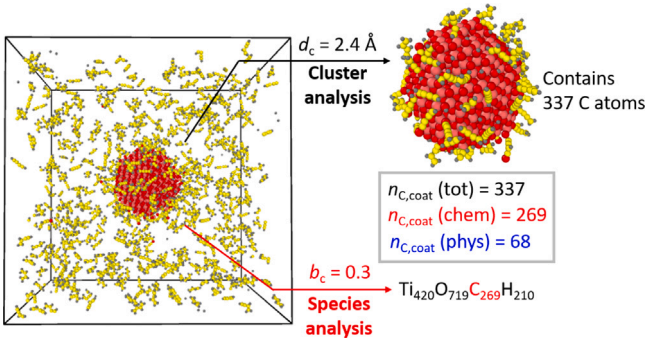

Fig. 2. Illustration of the approach to differentiating between physically coated carbon atoms and chemically coated carbon atoms. The snapshot of 600 C4 molecules/radicals (Case 4 in Fig. 1(b)) coating on the 3 nm titania nanoparticle ($Ti_{420}O_{728}$) at 2 ns, $T = 800$ K is taken as the example.

2.3. Identification of the coating mechanism — physical coating versus chemical coating

To quantitatively compare the carbon coating outcome with different hydrocarbon species at different temperatures, we tracked the number of C atoms that are coated on the titania nanoparticle ($n_{C,coat}$) during each simulation. The total $n_{C,coat}$ on the particle at a certain time is taken as the number of C atoms contained in the largest cluster (in terms of the total number of atoms in a cluster) within the simulation box, which can be determined by performing cluster analysis with a predefined atomic distance cutoff d_c. Any two atoms with a distance between them less than d_c are considered to belong to one cluster. Our previous work has shown that 2.4 Å is a proper cutoff to identify whether an oxygen atom is coordinated to a titanium atom in a titania nanoparticle [70,71], thus, $d_c = 2.4$ Å is chosen to perform the cluster analysis. Take 600 C4 molecules/radicals coating on a 3 nm titania nanoparticle (Case 4 in Fig. 1(b)) as an example. Figure 2 illustrates the snapshot after carbon coating at 800 K for 2 ns. Cluster analysis shows that the largest cluster contains 1760 atoms in total and 337 of them are C atoms, which indicates that 337 carbon atoms are coated on the titania nanoparticle at 2 ns.

As mentioned earlier in Section 2.1, ReaxFF depends on the bond-order description so it can describe bond formation and dissociation between any two atoms. Therefore, we are able to further examine if the coated carbon atom is formed through chemical bonds or physical interactions (i.e., van der Waals attraction). During the simulation, we used a bond-order cutoff $b_c = 0.3$ for species identification, which is a commonly used value based on experience and recommendation of many previous studies [37,72–76]. With $b_c = 0.3$, the largest species is recognized as $Ti_{420}O_{719}C_{269}H_{210}$. The number of carbon atoms in this largest species, i.e., 269, is regarded as the number of carbon atoms coated on the titania nanoparticle surface due to chemical interactions, that is, there are C–Ti or C–O bonds between the coated C_mH_n species and the titania nanoparticle surface. The number of C atoms that are physically coated on the particle (68) can then be calculated by subtracting the number of chemically coated C atoms (269) from the total number of coated C atoms (337). In this way, we managed to quantitatively describe the carbon coating outcome as well as compare the relative contribution of physical attraction and chemical bond formation to carbon coating.

3. Results and discussions

We first examine the dynamic process of carbon coating in Section 3.1. The coating tendencies in a wide range of temperatures and carbonaceous species types are summarized and compared in Section 3.2. For Cases 1–4 in Fig. 1(b), the coating tendencies among various carbonaceous species with the same number of C atoms are further compared in Section 3.3. Finally, the inception process of hydrocarbon species away from the central titania nanoparticle is examined in Section 3.4.

3.1. Dynamic process of carbon coating

Take 600 C4 molecules/radicals (120 C_4H_2 + 120 C_4H_3 + 120 C_4H_4 + 120 C_4H_5 + 120 C_4H_6, Case 4 in Fig. 1(b)) coating on the titania nanoparticle as an example. Figure 3 shows the temporal evolution of the number of C atoms coated ($n_{C,coat}$) on the titania nanoparticle at 800 K during 2 ns. According to Fig. 3, the coating process reaches an equilibrium state after ~1 ns, as the total number of coated C atoms

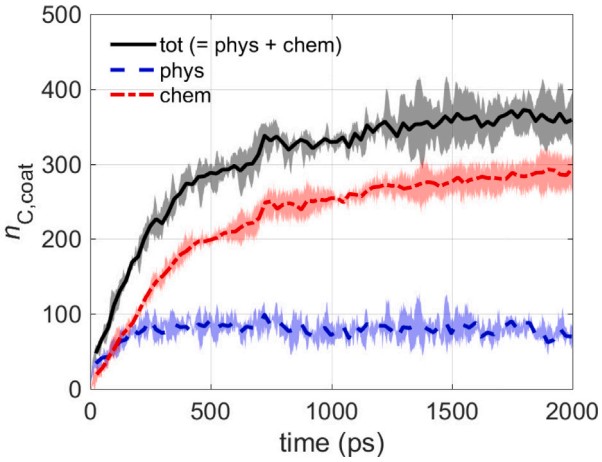

Fig. 3. The number of C atoms coated on a 3 nm titania nanoparticle ($Ti_{420}O_{728}$) versus time. The coating temperature is 800 K and the surrounding hydrocarbons are 600 C4 molecules/radicals (120 C_4H_2 + 120 C_4H_3 + 120 C_4H_4 + 120 C_4H_5 + 120 C_4H_6, Case 4 in Fig. 1(b)).“tot” represents the total number of coated C atoms. “phys” represents coated C atoms due to physical adsorption while “chem” represents coated C atoms by chemical adsorption. The presented curves represent the averaged values of three replica runs with different initial configurations. Uncertainties in the simulation results are determined as the standard deviation of three replica runs and are illustrated by the semi-transparent area around the curve.

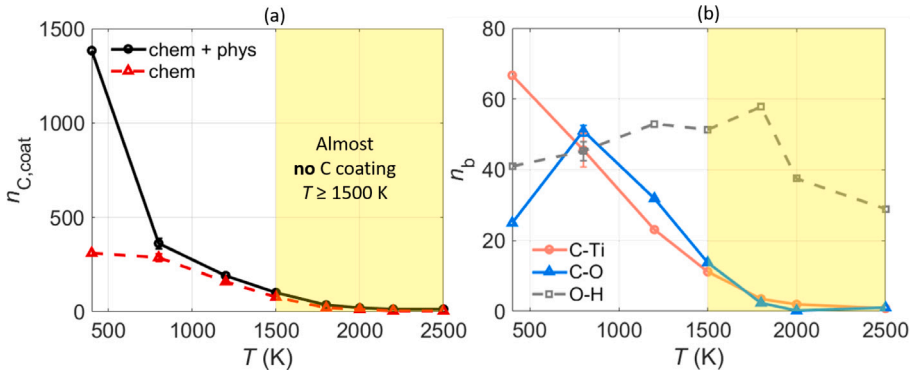

Fig. 4. The number of total (black solid line with circles) and chemically coated (red dashed line with triangles) C atoms (a); and the number of C–Ti, C–O and O–H bonds (b) versus temperature for 600 C4 molecules/radicals (120 C_4H_2 + 120 C_4H_3 + 120 C_4H_4 + 120 C_4H_5 + 120 C_4H_6, Case 4 in Fig. 1(b)) coating on a 3 nm titania nanoparticle ($Ti_{420}O_{728}$) in 2 ns. At each temperature, $n_{C,coat}$ is obtained by averaging the simulation results during 1950–2000 ps for each simulation condition. Error bars of $n_{C,coat}$ and n_b at 800 K are plotted based on the standard deviation of three replica runs with different initial configurations.

hardly changes with time after 1 ns. The blue-dashed line indicates that physical coating of C atoms reaches equilibrium in a much shorter period of time, i.e., in ~150 ps, while chemical coating of C atoms does not achieve equilibrium until 1 ns. Approximately 350 C atoms are coated on the titania nanoparticle in 1 ns, and most of them are coated through chemical adsorption, with only ~80 C atoms being physically adsorbed onto the nanoparticle. Our simulation results suggest that for 600 C4 molecules/radicals coating on the titania nanoparticle at 800 K, the amounts of physical interactions are much less than those of chemical interactions. This is because some of the C4 species such as C_4H_2 are highly reactive, and can form chemical bonds with the titania nanoparticle surface easily at 800 K, which will be discussed in more detail (see Fig. 5). In addition, C4 species do not have large molecular weights, which leads to physical interactions insignificant compared with the chemical interactions.

Figure 4 shows the simulation results of 600 C4 molecules/radicals coating on the titania nanoparticle at different temperatures. In Fig. 4(a), the number of coated C atoms ($n_{C,coat}$) at each temperature is obtained by averaging the simulation results during 1950–2000 ps. Since carbon coating reaches an equilibrium state after ~1 ns (as illustrated by Fig. 3), the averaged simulation results during 1950–2000 ps can reflect the carbon coating outcome at an equilibrium state. According to Fig. 4(a), the total $n_{C,coat}$ (denoted by the black solid line) decreases drastically with increasing temperature. The number of chemically coated C atoms begins to decrease rapidly when the temperature becomes higher than 800 K, while $n_{C,coat}$ at 400 K is close to the value at 800 K. At temperatures higher than 1500 K, C atoms can hardly coat on the titania nanoparticle, as marked by the yellow region in Fig. 4. The number of C–Ti bonds and C–O bonds are further tracked to examine the chemical adsorption in detail. In Fig. 4(b), the number of bonds (n_b) at each temperature is also obtained by averaging the simulation results during 1950–2000 ps. Figure 4(b) suggests that the formation of C–Ti bonds is most favorable at the lowest temperature being simulated, i.e., 400 K, while the number of C–O bonds achieves its maximum at a slightly higher temperature – 800 K. For temperatures higher than 800 K, both C–Ti bonds and C–O bonds reduce with temperature. When temperatures increase beyond 1800 K, there are almost no C–Ti bonds or C–O bonds left, which echos the results in Fig. 4(a) suggesting the number of chemically coated C atoms is nearly 0. The number of O–H bonds at different temperatures during carbon coating is also shown in Fig. 4, which is less temperature-dependent compared with C–Ti or C–O bonds. The observed O–H bond formation suggests that the titania nanoparticle can abstract a certain amount of H atoms from the surrounding hydrocarbons across a wide temperature range, which can promote the formation of carbonaceous clusters from the hydrocarbon molecule/radicals, as will be shown in Section 3.4.

Figure 5(a) shows the morphology of the titania nanoparticle after 2 ns coating with 600 C4 molecules/radicals at 800 K. Typical newly formed C–Ti and C–O bonds near the nanoparticle surface during the coating process are illustrated in Fig. 5(b), (c), and (d). Fig. 5(b)

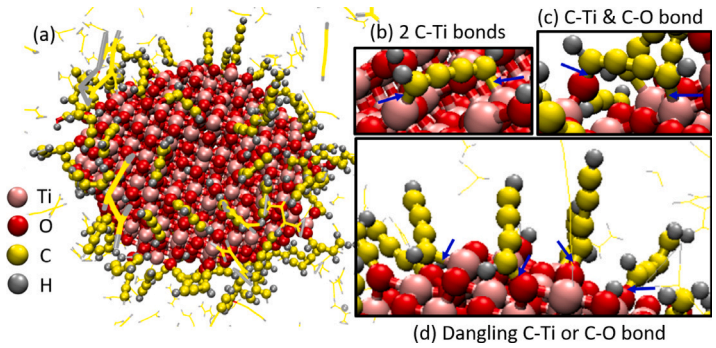

Fig. 5. (a) Illustration of the chemical bonds formed after 600 C4 molecules/radicals coating on a 3 nm titania nanoparticle ($Ti_{420}O_{728}$) at 800 K (120 C_4H_2 + 120 C_4H_3 + 120 C_4H_4 + 120 C_4H_5 + 120 C_4H_6, Case 4 in Fig. 1(b)) for 2 ns; (b), (c) and (d) are snapshots obtained by zooming in local regions of the particle surface to demonstrate the newly formed bonds during carbon coating. (b) shows two C–Ti bonds formed between one C_4H_2 molecule and two Ti atoms on the particle surface; (c) shows one C–Ti bond and one C–O bond formed between one C_4H_2 molecule and the particle surface; (d) shows dangling C–Ti bonds or C–O bonds formed between hydrocarbon species and the particle surface. (For interpretation of the references to color in this figure legend, the reader is referred to the web version of this article.)

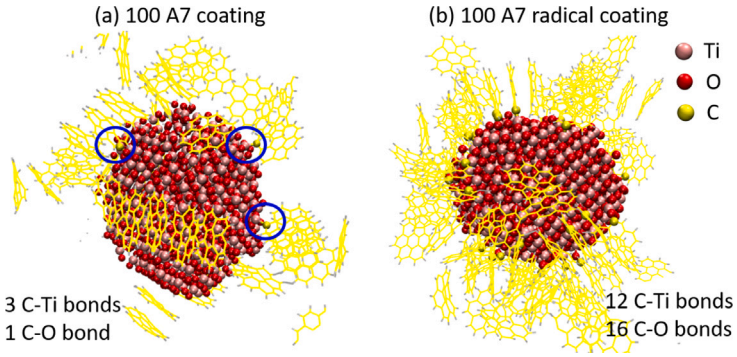

Fig. 6. Snapshots of 100 A7 molecules (a) and 100 A7 radicals (b) coating on a 3 nm titania nanoparticle ($Ti_{420}O_{728}$) at 1200 K for 2 ns, respectively. C atoms forming C–Ti bonds or C–O bonds with surface Ti/O atoms are highlighted as yellow spheres; while other C atoms and H atoms are shown by lines for clarity. (For interpretation of the references to color in this figure legend, the reader is referred to the web version of this article.)

shows one C_4H_2 molecule forming two C–Ti bonds with the titania nanoparticle surface, while Fig. 5(c) shows one C_4H_2 molecule forming one C–Ti bond and one C–O bond with the nanoparticle surface. This suggests that the two carbon atoms at both ends of a C_4H_2 molecule are highly reactive and they tend to form C–Ti/O bonds with surface Ti or O atoms. Since two bonds are formed between the C_4H_2 molecule and the nanoparticle surface in Figs. 5(b) and 5(c), the C_4H_2 molecule clings to the surface of the nanoparticle tightly. By contrast, Fig. 5(d) demonstrates another kind of bonding type, where one C4 species only forms one C–Ti or C–O bond with the nanoparticle surface, resulting in the dangling C–Ti or C–O bonds. Note that although species other than C_4H_2 have been observed to chemically coat on the titania nanoparticle surface, C_4H_2 is the dominant species in the carbonaceous shell enclosing the particle. The competition among different aliphatic species with the same number of C atoms coating on the titania nanoparticle will be discussed in further detail in Section 3.3.

Figure 6 further illustrates the morphology of the carbon-coated titania nanoparticle after 2 ns coating with 100 surrounding A7 molecules (100 $C_{24}H_{12}$, Case 7a in Fig. 1(b)) or radicals (100 $C_{24}H_{11}$, Case 7b in Fig. 1(b)). Instead of being parallel to the nanoparticle surface, most A7 molecules/radicals tend to be perpendicular to the surface of the titania nanoparticle. Since A7 radicals are born with a reactive σ-radical site, their chemisorption on the particle surface is much easier than its counterpart — stable A7 molecules. As shown in Fig. 6, only three C–Ti bonds and one C–O bond are formed between A7 molecules and the titania nanoparticle surface. By contrast, 12 C–Ti bonds and 16 C–O bonds are formed between A7 radicals and the titania nanoparticle.

3.2. Carbon coating versus hydrocarbon species size and temperature

To clarify the coating tendencies of different hydrocarbon species at various temperatures, we summarized the number of physically and chemically coated C atoms in Fig. 7(a) and 7(b), respectively. The number of coated carbon atoms ($n_{C,coat}$ in each cell) is obtained by averaging the simulation results during 1950–2000 ps. Figure 7(a) suggests that physical coating is dominated at low temperatures for large C_mH_n species, while Fig. 7(b) shows chemical coating has no general preference in the size of hydrocarbon species. Compared with the short chain C1–C4 aliphatic species, PAH molecules such as benzene (A1), coronene (A7), and ovalene (A10) do not tend to chemically coat on the particle surface at $T < 1200$ K, due to the fact that PAH molecules are rather stable and not reactive enough. If the surrounding hydrocarbons are PAH radicals rather than PAH molecules, the number of chemically coated C atoms increases significantly, see e.g., A1 radical and A7 radical coating at 400, 800 and 1200 K in Fig. 7(b). However, it is noteworthy that the number of chemically coated C atoms of A4 coating on the titania nanoparticle at 800 K is abnormally larger than that of the other three PAH molecules, i.e., A1, A7, and A10 coating on the titania nanoparticle at 800 K. We performed three replica runs with different initial configurations for A4 coating on the titania nanoparticle at 800 K, suggesting that the abnormally large chemical $n_{C,coat}$ is less likely to be caused by the random error. Detailed simulation results of the three replica runs can be found in Table S2 in the Supporting Information. Figure 7(b) also suggests that high temperatures ($T \geq 1500$ K) can prevent carbon atoms from being chemically coated on the titania nanoparticle surface regardless of size of the hydrocarbon species.

To compare whether the hydrocarbons prefer to be chemisorbed on the surface Ti-atomic sites or on the surface O-atomic sites, we

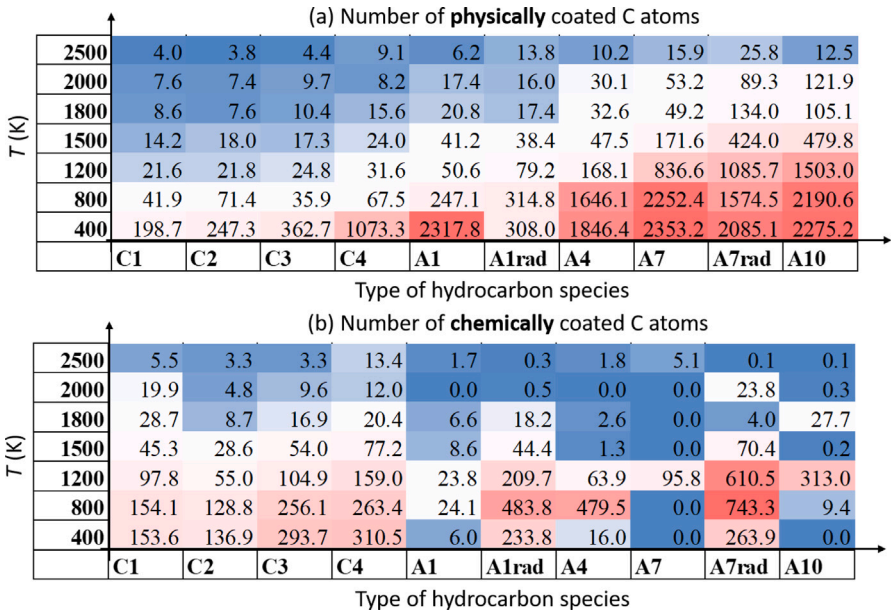

Fig. 7. The number of physically (a) and chemically (b) coated C atoms on a 3 nm titania nanoparticle ($Ti_{420}O_{728}$) with different surrounding hydrocarbons at various temperatures. $n_{C,coat}$ in each cell is obtained by averaging the simulation results during 1950–2000 ps under corresponding simulation condition. For easy comparison, the cells are colored in blue–white–red scale based on the value of $n_{C,coat}$ — The darker the red, the larger the $n_{C,coat}$; while the darker the blue, the smaller the $n_{C,coat}$; white color represents $n_{C,coat}$ in between. (For interpretation of the references to color in this figure legend, the reader is referred to the web version of this article.)

tracked the time evolution of the number of C–Ti bonds ($n_{b,C-Ti}$) and the number of C–O bonds ($n_{b,C-O}$) throughout the carbon coating simulation. $n_{b,C-Ti}$ and $n_{b,C-O}$ for all different hydrocarbon species at temperatures from 400 K to 2500 K are summarized in Fig. 8(a) and Fig. 8(b), respectively. $n_{b,C-Ti}$ and $n_{b,C-O}$ in each cell in Fig. 8 are obtained by averaging the simulation results during 1950–2000 ps. Figure 8 indicates that neither C–Ti bonds nor C–O bonds prefer to form at temperatures higher than 1500 K, which is consistent with the results in Fig. 7(b); While at $T \leq 1500$ K, in general, the C–Ti bond is easier to form than the C–O bond. Figure 8 also shows that aliphatic species containing 1–4 C atoms form more C–Ti and C–O bonds comparing with PAH species. For coated C1–C4 species, Fig. 8(a) shows that the most favorable temperature for the formation of C–Ti bond is close to 400 K, while the formation of C–O bonds favors a higher temperature of approximately 800 K. Compared with those C1–C4 aliphatic species, PAH molecules are too stable to form C–Ti bond or C–O bond with the titania nanoparticle. In order to be chemisorbed on the surface Ti/O atomic sites, one H atom on the edge of the PAH molecule has to be abstracted first to form a reactive C site. In contrast, PAH radicals can form a considerable number of C–Ti or C–O bonds with the titania nanoparticle surface, suggesting that the barrier for chemisorption of PAH molecules is the generation of the reactive C sites.

3.3. Coating tendency comparison of aliphatic hydrocarbons

To obtain coating tendencies of the C1–C4 aliphatic hydrocarbons, the coating process of a mixture of C1, C2, C3 and C4 gaseous species (as listed in Fig. 1(b)) onto the titania nanoparticle is simulated. A mixture of C_mH_n species is selected to mimic the gaseous species in typical flame environments. Besides, this approach allows us to examine the coating tendencies of aliphatic species with different C/H ratios by tracking the origin of carbon atoms coated on the titania nanoparticle. The origin of C source, i.e., the contribution of each hydrocarbon species to the C-coating layer, can be difficult to track through experiments, yet such information can be easily identified based on atom identifiers during MD simulations.

Figure 9(a) shows the temporal evolution of the number of C atoms coated on the titania nanoparticle at 800 K with 1200 C2 species (400 C_2H_2 + 400 C_2H_3 + 400 C_2H_4, Case 2 in Fig. 1(b)). The coated C atoms are classified into three groups according to their origins from the three surrounding C2 species, i.e., C_2H_2, C_2H_3, and C_2H_4. As illustrated in Fig. 9(a), most of C atoms consisting of the carbon layer come from C_2H_2, suggesting that C_2H_2 is more easily to be chemisorbed on the titania nanoparticle surface compared with C_2H_3 and C_2H_4. It is noteworthy that although C_2H_2 as a molecule does not have any unpaired electron, it has a higher coating tendency than C_2H_3 as a radical. Among the three C2 species, C_2H_4 has the least coating capability, which is reasonable as C_2H_4 is the most stable species. Based on the results in Fig. 9(a), we suspect that the C–C triple bond in a hydrocarbon species may correspond to a higher carbon coating tendency. This inference is supported by the simulation results of Case 4, i.e., 600 C4 species (120 C_4H_2 + 120 C_4H_3 + 120 C_4H_4 + 120 C_4H_5 + 120 C_4H_6) coating on the titania nanoparticle. As suggested by Fig. 9(b), the C_4H_2 molecule, which has two C–C triple bonds, owns the highest coating capability, followed by C_4H_3 radical and C_4H_4 molecule, which have one C–C triple bond; The C_4H_5 radical and C_4H_6 molecule, which do not have C–C triple bond, have the least coating capability. Such finding can be a helpful guide on choosing proper carbon precursors when synthesizing carbon coated titania nanoparticles by flame aerosol technology, although more experimental data in future studies are desired to verify our simulation results.

3.4. Inception of hydrocarbon species

For a complex system containing both titania nanoparticles and hydrocarbon species, C_mH_n may coat on the surface of metal oxide nanoparticle, as we have illustrated in Figs. 5 and 6, however, it is also possible that C_mH_n molecules/radicals themselves gather together forming larger carbonaceous clusters [11,19], which is similar to the inception of soot under fuel-rich flame conditions. To quantitatively characterize the formation and growth of carbonaceous clusters away from the titania nanoparticle surface, temporal evolutions of the following two properties are tracked. The first one is the number of C atoms in the largest hydrocarbon species, denoted as $n_{C,max}$. Since the growth of hydrocarbon species is accompanied by the formation of C–C bonds, $n_{C,max}$ corresponds to the clustering tendency of hydrocarbon species. The total number of C atoms in all carbonaceous clusters is also tracked, so as to take all other carbonaceous clusters into account besides the

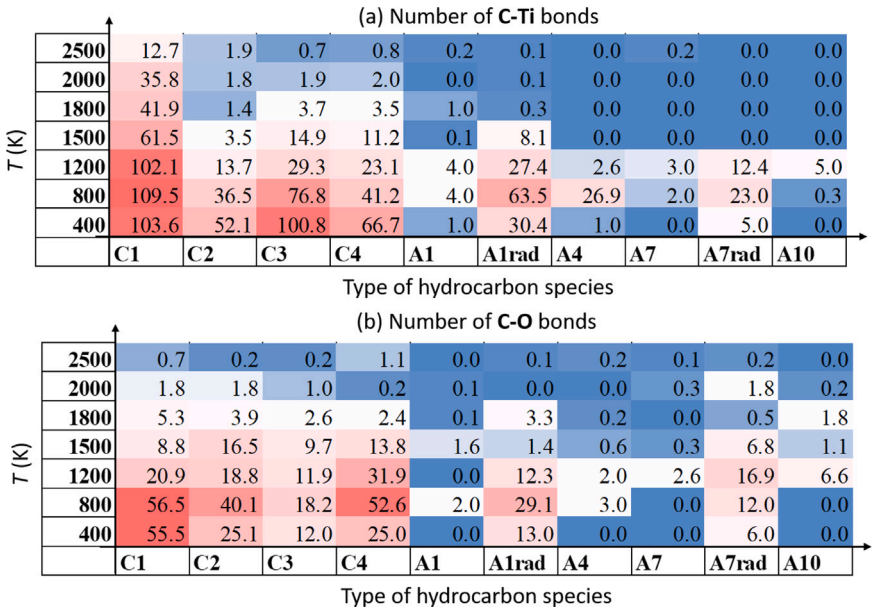

Fig. 8. The number of C–Ti bonds (a) and C–O bonds (b) formed after different hydrocarbon species coating on a 3 nm titania nanoparticle ($Ti_{420}O_{728}$) at various temperatures for 2 ns. The number of bonds (n_b) in each cell is obtained by averaging the simulation results during 1950–2000 ps under corresponding simulation condition. For easy comparison, the cells are colored in blue–white–red scale based on the value of n_b — The darker the red, the larger the n_b; While the darker the blue, the smaller the n_b; White color represents n_b in between. (For interpretation of the references to color in this figure legend, the reader is referred to the web version of this article.)

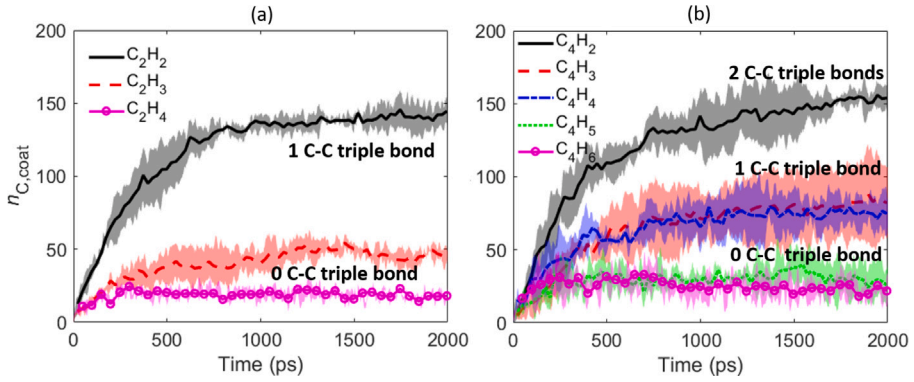

Fig. 9. The number of C atoms coated on a 3 nm titania nanoparticle ($Ti_{420}O_{728}$) originating from different surrounding hydrocarbon species: (a) C_2H_2, C_2H_3, C_2H_4 (Case 2 in Fig. 1(b)); and (b) C_4H_2, C_4H_3, C_4H_4, C_4H_5, C_4H_6 (Case 4 in Fig. 1(b)) at 800 K versus time. The presented curves represent the averaged values of three replica runs with different initial configurations. Uncertainties in the simulation results are determined as the standard deviation of three replica runs and are illustrated by the semi-transparent area around the curve.

largest one. A carbonaceous cluster is defined if it is larger than the dimer of the initial hydrocarbon molecules. For example, if initially the titania nanoparticle is surrounded by 600 C4 molecules/radicals (Case 4 in Fig. 1(b)), then throughout the 2 ns coating simulation, any $C_mH_nO_l$ species with $m \geq 8 (= 2 \times 4)$ is regarded as a carbonaceous cluster. This is equivalent to taking species larger than the size of a dimer of the initial hydrocarbon species as a carbonaceous cluster. In forming such a carbonaceous cluster, at least one C–C bond is formed between two hydrocarbon monomers.

Figure 10(a) illustrates the temporal evolution of the number of C atoms in the largest hydrocarbon species, i.e., $n_{C,max}$, during 600 C4 species coating on the 3 nm titania nanoparticle (Case 4 in Fig. 1(b)) at various temperatures. According to Fig. 10(a), at 400 K, $n_{C,max} = 4$ throughout the 2 ns simulation, indicating no C–C bond formation. In fact, Fig. 10(a) suggests that C–C bond hardly forms at $T \leq 1200$ K while a moderate number of C–C bonds has formed at 1500–1800 K, where the largest hydrocarbon species contains ~30 carbon atoms, corresponding to about 8 monomers. By contrast, C–C bond formation is significantly promoted at temperatures higher than 2000 K. At 2500 K, the largest hydrocarbon species almost contains 100 C atoms. The total number of C atoms in carbonaceous clusters in Fig. 10(b) further supports the conclusion that C–C bond formation is promoted with increasing temperature. Both Figs. 10(a) and 10(b) indicate C–C bond tends to form at $T \geq 1500$ K, which however, is outside the optimal temperature range ($T \leq 1200$ K) for carbon to be coated on the titania nanoparticle as has been determined in Section 3.2 (see e.g., Fig. 7 and Fig. 8). This indicates that high temperatures ($T \geq 1500$ K) promote the formation and growth of larger hydrocarbon species, yet they can hardly coat on the titania nanoparticle at such high temperatures.

Similar temperature dependency of the formation and growth of carbonaceous clusters has been found for carbon coating with all other hydrocarbon species. The number of C atoms in carbonaceous clusters ($n_{C,cluster}$) outside the C-coating layer with various initial hydrocarbon species at different temperatures is shown in Fig. 11. $n_{C,cluster}$ in each cell shown in Fig. 11 is obtained by averaging the results during 1950–2000 ps. Figure 11 shows that opposite to the temperature dependency of the carbon coating process, carbonaceous clusters tend to form at high temperatures, i.e., $T \geq 1500$ K, regardless of the initial hydrocarbon species. This could possibly explain the relatively thin thickness of

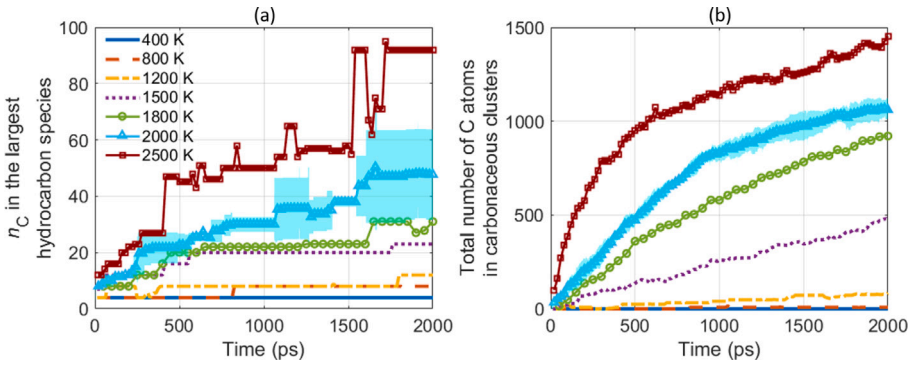

Fig. 10. The number of carbon atoms in the largest hydrocarbon species (a); and the total number of C atoms in carbonaceous clusters (i.e., $C_mH_nO_l$ ($m \geq 8$) species) (b) versus time during 600 C4 molecules/radicals coating on a 3 nm titania nanoparticle ($Ti_{420}O_{728}$) at various temperatures. For T = 2000 K, the presented curves represent the averaged values of three replica runs with different initial configurations. Uncertainties in the simulation results are determined as the standard deviation of three replica runs and are illustrated by the semi-transparent area around the curve.

Number of C atoms in carbonaceous clusters

T (K)	C1	C2	C3	C4	A1	A1 rad	A4	A7	A7rad	A10
2500	474.2	912.8	1528.9	1417.5	407.3	1440.9	323.8	311.4	1306.6	703.9
2000	356.8	434.8	1364.3	1011.1	128.6	1734.7	160	192	1263.5	320.4
1800	313.3	281.8	1145.3	920.8	67.9	1655.3	209.9	96	1073	255.4
1500	281.2	104.7	578.4	476.4	48	1321.7	96	96	768	122.6
1200	202.7	32.1	219.8	76.5	11	745.9	0	0	480	0
800	32.9	4	84	8	0	501.8	0	0	624	0
400	1.2	0	0	0	0	156.9	0	0	144	0

Type of hydrocarbon species

Fig. 11. The total number of carbon atoms in carbonaceous clusters ($n_{C,cluster}$) after different hydrocarbon species coating on a 3 nm titania nanoparticle ($Ti_{420}O_{728}$) at various temperatures for 2 ns. The number of C atoms in carbonaceous clusters ($n_{C,cluster}$ in each cell is obtained by averaging the simulation results during 1950–2000 ps) under corresponding simulation conditions. For easy comparison, the cells are colored in blue–white–red scale based on the value of $n_{C,cluster}$ — The darker the red, the larger the $n_{C,cluster}$; While the darker the blue, the smaller the $n_{C,cluster}$; White color represents $n_{C,cluster}$ in between. (For interpretation of the references to color in this figure legend, the reader is referred to the web version of this article.)

the carbon coating layer of the carbon coated titania nanocomposite obtained by flame aerosol synthesis [19,26].

4. Conclusions

In this study, we performed ReaxFF MD simulations to provide atomic insights into the initial stage of carbon coating on the nanoparticle in the context of gas-phase synthesized functional nanomaterials. Eighteen typical hydrocarbon species in flames, including chain aliphatic species with 1–4 C atoms and aromatic species with 1–10 aromatic rings were selected as carbon source for coating and their coating performance on a 3 nm titania nanoparticle was simulated for 2 ns under different temperatures ranging from 400 K to 2500 K. Main conclusions drawn from this work can be summarized as follows:

(1) During the process of hydrocarbon species coating on a titania nanoparticle in flames, the titania nanoparticle serves not only as a nucleus for physical condensation of surrounding C_mH_n species, but also participates in chemical reactions. The surface Ti/O atoms of the titania nanoparticle can form C–Ti and C–O bonds with the hydrocarbon species attached to the nanoparticle surface. Besides, O atoms on the surface of the titania nanoparticle can abstract H atoms from the surrounding hydrocarbon species.

(2) The optimal temperature range for carbon coating is $T \leq$ 1200 K, as both C–Ti bonds and C–O bonds become unstable at higher temperatures. In contrast, at temperatures higher than 1500 K, instead of coating on the surface of the titania nanoparticle, the hydrocarbon species tend to gather themselves to form larger carbonaceous species, because the formation of C–C bonds is significantly promoted at such high temperatures.

(3) During flame aerosol synthesis of carbon coated titania nanocomposites where the hydrocarbon fuel serves as the carbon source, a carbon coating mechanism is proposed based on our simulation results as follows: Small aliphatic species coat on the titania nanoparticle surface by forming C–Ti or C–O bonds with nanoparticle, while PAH species attach to particle surface mainly through physical adsorption. Although PAH radicals can also chemically bond onto the titania nanoparticle surface, physical adsorption on the titania nanoparticle surface is considered to be the major coating routes for PAH species, since the concentrations of PAH radicals are generally much smaller than those of PAH molecules.

(4) Coating tendency of chain aliphatic species is found to be closely related to the number of carbon–carbon triple bonds in a certain species. The more the number of C–C triple bonds a species has, the more readily it can be coated on the titania nanoparticle surface.

CRediT authorship contribution statement

Dingyu Hou: Conceptualization, Methodology, Software, Investigation, Data curation, Visualization, Writing – original draft. **Qian Mao:** Methodology, Software, Investigation, Writing – review & editing. **Yihua Ren:** Conceptualization, Supervision, Methodology, Writing – review & editing. **Kai H. Luo:** Conceptualization, Supervision, Funding acquisition, Resources, Investigation, Project administration, Writing – review & editing.

Declaration of competing interest

The authors declare that they have no known competing financial interests or personal relationships that could have appeared to influence the work reported in this paper.

Acknowledgments

This work was supported by the UK Engineering and Physical Sciences Research Council (EPSRC) under Grant Nos. EP/R029598/1 and EP/T015233/1. This work made use of computational support by CoSeC, the Computational Science Centre for Research Communities, through UKCOMES. Q.M. and Y. R. acknowledge Alexander von Humboldt Foundation.

Appendix A. Supplementary data

Supplementary material related to this article can be found online at https://doi.org/10.1016/j.carbon.2022.09.002.

References

[1] M. Inagaki, Carbon coating for enhancing the functionalities of materials, Carbon 50 (9) (2012) 3247–3266.
[2] A. Chakraborty, S. Kunnikuruvan, S. Kumar, B. Markovsky, D. Aurbach, M. Dixit, D.T. Major, Layered cathode materials for lithium-ion batteries: Review of computational studies on $LiNi_{1-x-y}Co_xMn_yO_2$ and $LiNi_{1-x-y}Co_xAl_yO_2$, Chem. Mater. 32 (3) (2020) 915–952.
[3] P. Poizot, S. Laruelle, S. Grugeon, L. Dupont, J. Tarascon, Nano-sized transition-metal oxides as negative-electrode materials for lithium-ion batteries, Nature 407 (6803) (2000) 496–499.
[4] M.V. Reddy, G. Subba Rao, B. Chowdari, Metal oxides and oxysalts as anode materials for Li ion batteries, Chem. Rev. 113 (7) (2013) 5364–5457.
[5] G. Zhou, D.-W. Wang, F. Li, L. Zhang, N. Li, Z.-S. Wu, L. Wen, G.Q. Lu, H.-M. Cheng, Graphene-wrapped Fe_3O_4 anode material with improved reversible capacity and cyclic stability for lithium ion batteries, Chem. Mater. 22 (18) (2010) 5306–5313.
[6] S. Yang, Y. Sun, L. Chen, Y. Hernandez, X. Feng, K. Müllen, Porous iron oxide ribbons grown on graphene for high-performance lithium storage, Sci. Rep. 2 (1) (2012) 1–7.
[7] Y.N. Ko, S.B. Park, S.H. Choi, Y.C. Kang, One-pot synthesis of manganese oxide-carbon composite microspheres with three dimensional channels for Li-ion batteries, Sci. Rep. 4 (1) (2014) 1–7.
[8] A.K. Padhi, K.S. Nanjundaswamy, J.B. Goodenough, Phospho-olivines as positive-electrode materials for rechargeable lithium batteries, J. Electrochem. Soc. 144 (4) (1997) 1188.
[9] J. Hong, C. Wang, X. Chen, S. Upreti, M.S. Whittingham, Vanadium modified $LiFePO_4$ cathode for Li-ion batteries, Electrochem. Solid-State Lett. 12 (2) (2008) A33.
[10] C. He, S. Wu, N. Zhao, C. Shi, E. Liu, J. Li, Carbon-encapsulated Fe_3O_4 nanoparticles as a high-rate lithium ion battery anode material, ACS Nano 7 (5) (2013) 4459–4469.
[11] O. Waser, R. Büchel, A. Hintennach, P. Novák, S.E. Pratsinis, Continuous flame aerosol synthesis of carbon-coated nano-$LiFePO_4$ for Li-ion batteries, J. Aerosol Sci. 42 (10) (2011) 657–667.
[12] X. Wang, Z. Feng, J. Huang, W. Deng, X. Li, H. Zhang, Z. Wen, Graphene-decorated carbon-coated $LiFePO_4$ nanospheres as a high-performance cathode material for lithium-ion batteries, Carbon 127 (2018) 149–157.
[13] X. Wang, J. Zhang, X. Kong, X. Huang, B. Shi, Increasing rigidness of carbon coating for improvement of electrochemical performances of Co_3O_4 in Li-ion batteries, Carbon 104 (2016) 1–9.
[14] Y.K. Kim, S.M. Sharker, I. In, S.Y. Park, Surface coated fluorescent carbon nanoparticles/TiO_2 as visible-light sensitive photocatalytic complexes for antifouling activity, Carbon 103 (2016) 412–420.
[15] M. Inagaki, F. Kojin, B. Tryba, M. Toyoda, Carbon-coated anatase: The role of the carbon layer for photocatalytic performance, Carbon 43 (8) (2005) 1652–1659.
[16] R. Koc, Kinetics and phase evolution during carbothermal synthesis of titanium carbide from carbon-coated Titania powder, J. Eur. Ceram. Soc. 17 (11) (1997) 1309–1315.
[17] G. Swift, R. Koc, Formation studies of TiC from carbon coated TiO_2, J. Mater. Sci. 34 (13) (1999) 3083–3093.
[18] R. Koc, C. Meng, G. Swift, Sintering properties of submicron TiC powders from carbon coated titania precursor, J. Mater. Sci. 35 (12) (2000) 3131–3141.
[19] H.K. Kammler, S.E. Pratsinis, Carbon-coated titania nanostructured particles: Continuous, one-step flame-synthesis, J. Mater. Res. 18 (11) (2003) 2670–2676.
[20] G.A. Kelesidis, S.E. Pratsinis, A perspective on gas-phase synthesis of nanomaterials: Process design, impact and outlook, Chem. Eng. J. 421 (2021) 129884.
[21] S. Li, Y. Ren, P. Biswas, D.T. Stephen, Flame aerosol synthesis of nanostructured materials and functional devices: Processing, modeling, and diagnostics, Prog. Energy Combust. Sci. 55 (2016) 1–59.
[22] F. Meierhofer, U. Fritsching, Synthesis of metal oxide nanoparticles in flame sprays: Review on process technology, modeling, and diagnostics, Energy Fuels 35 (7) (2021) 5495–5537.
[23] L. Mädler, H. Kammler, R. Mueller, S.E. Pratsinis, Controlled synthesis of nanostructured particles by flame spray pyrolysis, J. Aerosol Sci. 33 (2) (2002) 369–389.
[24] S.E. Pratsinis, History of manufacture of fine particles in high-temperature aerosol reactors, Aerosol Sci. Technol. Hist. Rev. (2011) 475–507.
[25] H.K. Kammler, R. Mueller, O. Senn, S.E. Pratsinis, Synthesis of silica-carbon particles in a turbulent H_2-air flame aerosol reactor, AIChE J. 47 (7) (2001) 1533–1543.
[26] Y. Ren, K. Ran, S. Kruse, J. Mayer, H. Pitsch, Flame synthesis of carbon metal-oxide nanocomposites in a counterflow burner, Proc. Combust. Inst. 38 (1) (2021) 1269–1277.
[27] F.O. Ernst, R. Büchel, R. Strobel, S.E. Pratsinis, One-step flame-synthesis of carbon-embedded and-supported platinum clusters, Chem. Mater. 20 (6) (2008) 2117–2123.
[28] C. Qi, S. Li, Z. Yang, Z. Xiao, L. Zhao, F. Yang, G. Ning, X. Ma, C. Wang, J. Xu, et al., Suitable thickness of carbon coating layers for silicon anode, Carbon 186 (2022) 530–538.
[29] H. Michelsen, Probing soot formation, chemical and physical evolution, and oxidation: A review of in situ diagnostic techniques and needs, Proc. Combust. Inst. 36 (1) (2017) 717–735.
[30] T.P. Senftle, S. Hong, M.M. Islam, S.B. Kylasa, Y. Zheng, Y.K. Shin, C. Junkermeier, R. Engel-Herbert, M.J. Janik, H.M. Aktulga, et al., The ReaxFF reactive force-field: Development, applications and future directions, Npj Comput. Mater. 2 (1) (2016) 1–14.
[31] M.E. Tuckerman, Ab initio molecular dynamics: Basic concepts, current trends and novel applications, J. Phys.: Condens. Matter 14 (50) (2002) R1297.
[32] Q. Chu, K.H. Luo, D. Chen, Exploring complex reaction networks using neural network-based molecular dynamics simulation, J. Phys. Chem. Lett. 13 (2022) 4052–4057.
[33] Q. Mao, A.C. Van Duin, K. Luo, Formation of incipient soot particles from polycyclic aromatic hydrocarbons: A ReaxFF molecular dynamics study, Carbon 121 (2017) 380–388.
[34] J. Wei, A. Ostadhossein, S. Li, M. Ihme, Kinetics for the hydrolysis of $Ti(OC_3H_7)_4$: A molecular dynamics simulation study, Proc. Combust. Inst. 38 (1) (2021) 1433–1440.
[35] Q. Chu, B. Shi, L. Liao, K.H. Luo, N. Wang, C. Huang, Ignition and oxidation of core–shell Al/Al_2O_3 nanoparticles in an oxygen atmosphere: Insights from molecular dynamics simulation, J. Phys. Chem. C 122 (51) (2018) 29620–29627.
[36] M. Feng, X.Z. Jiang, K.H. Luo, A reactive molecular dynamics simulation study of methane oxidation assisted by platinum/graphene-based catalysts, Proc. Combust. Inst. 37 (4) (2019) 5473–5480.
[37] D. Hou, M. Feng, J. Wei, Y. Wang, A.C. van Duin, K.H. Luo, A reactive force field molecular dynamics study on the inception mechanism of titanium tetraisopropoxide (TTIP) conversion to titanium clusters, Chem. Eng. Sci. (2022) 117496.
[38] S. Hong, A.C. van Duin, Atomistic-scale analysis of carbon coating and its effect on the oxidation of aluminum nanoparticles by ReaxFF-molecular dynamics simulations, J. Phys. Chem. C 120 (17) (2016) 9464–9474.
[39] W.J. Mortier, S.K. Ghosh, S. Shankar, Electronegativity-equalization method for the calculation of atomic charges in molecules, J. Am. Chem. Soc. 108 (15) (1986) 4315–4320.
[40] A.C. Van Duin, S. Dasgupta, F. Lorant, W.A. Goddard, ReaxFF: A reactive force field for hydrocarbons, J. Phys. Chem. A 105 (41) (2001) 9396–9409.
[41] K. Chenoweth, A.C. Van Duin, W.A. Goddard, ReaxFF reactive force field for molecular dynamics simulations of hydrocarbon oxidation, J. Phys. Chem. A 112 (5) (2008) 1040–1053.
[42] K. Ganeshan, Y.K. Shin, N.C. Osti, Y. Sun, K. Prenger, M. Naguib, M. Tyagi, E. Mamontov, D.-e. Jiang, A.C. Van Duin, Structure and dynamics of aqueous electrolytes confined in 2D-$TiO_2/Ti_3C_2T_2$ MXene heterostructures, ACS Appl. Mater. Interfaces 12 (52) (2020) 58378–58389.
[43] J.L. Achtyl, R.R. Unocic, L. Xu, Y. Cai, M. Raju, W. Zhang, R.L. Sacci, I.V. Vlassiouk, P.F. Fulvio, P. Ganesh, et al., Aqueous proton transfer across single-layer graphene, Nature Commun. 6 (1) (2015) 1–7.
[44] S.-Y. Kim, A.C. Van Duin, J.D. Kubicki, Molecular dynamics simulations of the interactions between TiO_2 nanoparticles and water with Na^+ and Cl^-, methanol, and formic acid using a reactive force field, J. Mater. Res. 28 (3) (2013) 513–520.
[45] N.C. Osti, M. Naguib, A. Ostadhossein, Y. Xie, P.R. Kent, B. Dyatkin, G. Rother, W.T. Heller, A.C. Van Duin, Y. Gogotsi, et al., Effect of metal ion intercalation on the structure of MXene and water dynamics on its internal surfaces, ACS Appl. Mater. Interfaces 8 (14) (2016) 8859–8863.
[46] N.C. Osti, M. Naguib, K. Ganeshan, Y.K. Shin, A. Ostadhossein, A.C. Van Duin, Y. Cheng, L.L. Daemen, Y. Gogotsi, E. Mamontov, et al., Influence of metal ions intercalation on the vibrational dynamics of water confined between MXene layers, Phys. Rev. Mater. 1 (6) (2017) 065406.
[47] M. Raju, S.-Y. Kim, A.C. Van Duin, K.A. Fichthorn, ReaxFF reactive force field study of the dissociation of water on titania surfaces, J. Phys. Chem. C 117 (20) (2013) 10558–10572.

[48] M. Raju, A.C. Van Duin, K.A. Fichthorn, Mechanisms of oriented attachment of TiO_2 nanocrystals in vacuum and humid environments: Reactive molecular dynamics, Nano Lett. 14 (4) (2014) 1836–1842.
[49] M. Mojtabavi, A. VahidMohammadi, K. Ganeshan, D. Hejazi, S. Shahbazmohamadi, S. Kar, A.C. Van Duin, M. Wanunu, Wafer-scale lateral self-assembly of mosaic $Ti_3C_2T_x$ MXene monolayer films, ACS Nano 15 (1) (2021) 625–636.
[50] X. Sang, Y. Xie, D.E. Yilmaz, R. Lotfi, M. Alhabeb, A. Ostadhossein, B. Anasori, W. Sun, X. Li, K. Xiao, et al., In situ atomistic insight into the growth mechanisms of single layer 2D transition metal carbides, Nature Commun. 9 (1) (2018) 1–9.
[51] S.H. Overbury, A.I. Kolesnikov, G.M. Brown, Z. Zhang, G.S. Nair, R.L. Sacci, R. Lotfi, A.C. Van Duin, M. Naguib, Complexity of intercalation in MXenes: Destabilization of urea by two-dimensional titanium carbide, J. Am. Chem. Soc. 140 (32) (2018) 10305–10314.
[52] R. Lotfi, M. Naguib, D.E. Yilmaz, J. Nanda, A.C. Van Duin, A comparative study on the oxidation of two-dimensional Ti_3C_2 MXene structures in different environments, J. Mater. Chem. A 6 (26) (2018) 12733–12743.
[53] G. Plummer, B. Anasori, Y. Gogotsi, G.J. Tucker, Nanoindentation of monolayer $Ti_{n+1}C_nT_x$ MXenes via atomistic simulations: The role of composition and defects on strength, Comput. Mater. Sci. 157 (2019) 168–174.
[54] D. Zhang, M. Ashton, A. Ostadhossein, A.C. Van Duin, R.G. Hennig, S.B. Sinnott, Computational study of low interlayer friction in $Ti_{n+1}C_n$ (n =1, 2, and 3) MXene, ACS Appl. Mater. Interfaces 9 (39) (2017) 34467–34479.
[55] L. Martínez, R. Andrade, E.G. Birgin, J.M. Martínez, PACKMOL: A package for building initial configurations for molecular dynamics simulations, J. Comput. Chem. 30 (13) (2009) 2157–2164.
[56] C. Liu, J. Camacho, H. Wang, Phase equilibrium of TiO_2 nanocrystals in flame-assisted chemical vapor deposition, ChemPhysChem 19 (2) (2018) 180–186.
[57] R.D. Shannon, Phase transformation studies in TiO_2 supporting different defect mechanisms in vacuum-reduced and hydrogen-reduced rutile, J. Appl. Phys. 35 (11) (1964) 3414–3416.
[58] X. Chen, S.N. Hosseini, M.A. van Huis, Heating-induced transformation of anatase TiO_2 nanorods into rock-salt TiO nanoparticles: Implications for photocatalytic and gas-sensing applications, ACS Appl. Nano Mater. 5 (1) (2022) 1600–1606.
[59] N. Hansen, T.A. Cool, P.R. Westmoreland, K. Kohse-Höinghaus, Recent contributions of flame-sampling molecular-beam mass spectrometry to a fundamental understanding of combustion chemistry, Prog. Energy Combust. Sci. 35 (2) (2009) 168–191.
[60] L. Figura, F. Carbone, A. Gomez, Challenges and artifacts of probing high-pressure counterflow laminar diffusion flames, Proc. Combust. Inst. 35 (2) (2015) 1871–1878.
[61] F. Carbone, K. Gleason, A. Gomez, Pressure effects on incipiently sooting partially premixed counterflow flames of ethylene, Proc. Combust. Inst. 36 (1) (2017) 1395–1402.
[62] P. Desgroux, A. Faccinetto, X. Mercier, T. Mouton, D.A. Karkar, A. El Bakali, Comparative study of the soot formation process in a “nucleation” and a “sooting” low pressure premixed methane flame, Combust. Flame 184 (2017) 153–166.
[63] A. Bhargava, P.R. Westmoreland, Measured flame structure and kinetics in a fuel-rich ethylene flame, Combust. Flame 113 (3) (1998) 333–347.
[64] H. Wang, Formation of nascent soot and other condensed-phase materials in flames, Proc. Combust. Inst. 33 (1) (2011) 41–67.
[65] M. Commodo, K. Kaiser, G. De Falco, P. Minutolo, F. Schulz, A. D’Anna, L. Gross, On the early stages of soot formation: Molecular structure elucidation by high-resolution atomic force microscopy, Combust. Flame 205 (2019) 154–164.
[66] S. Plimpton, Fast parallel algorithms for short-range molecular dynamics, J. Comput. Phys. 117 (1) (1995) 1–19.
[67] H.M. Aktulga, J.C. Fogarty, S.A. Pandit, A.Y. Grama, Parallel reactive molecular dynamics: Numerical methods and algorithmic techniques, Parallel Comput. 38 (4–5) (2012) 245–259.
[68] W. Humphrey, A. Dalke, K. Schulten, VMD: Visual molecular dynamics, J. Mol. Graph. 14 (1) (1996) 33–38.
[69] A. Stukowski, Visualization and analysis of atomistic simulation data with OVITO – The open visualization tool, Modelling Simulation Mater. Sci. Eng. 18 (1) (2009) 015012.
[70] Y. Ren, Y. Zhang, Q. Mao, H. Pitsch, Amorphous-to-crystalline transition during sintering of nascent TiO_2 nanoparticles in gas-phase synthesis: A molecular dynamics study, J. Phys. Chem. C 124 (50) (2020) 27763–27771.
[71] Q. Mao, Y. Ren, K.H. Luo, S. Li, Sintering-induced phase transformation of nanoparticles: A molecular dynamics study, J. Phys. Chem. C 119 (51) (2015) 28631–28639.
[72] M. Feng, H. Li, Q. Mao, K.H. Luo, P. Hellier, Fundamental study on mechanisms of thermal decomposition and oxidation of aluminum hydride, J. Phys. Chem. C 123 (40) (2019) 24436–24445.
[73] M. Feng, H. Li, K.H. Luo, A molecular dynamics study on oxidation of aluminum hydride (AlH_3)/hydroxyl-terminated polybutadiene (HTPB) solid fuel, Proc. Combust. Inst. 38 (3) (2021) 4469–4476.
[74] Z. Bai, X.Z. Jiang, K.H. Luo, Effects of water on pyridine pyrolysis: A reactive force field molecular dynamics study, Energy 238 (2022) 121798.
[75] S. Agrawalla, A.C. Van Duin, Development and application of a ReaxFF reactive force field for hydrogen combustion, J. Phys. Chem. A 115 (6) (2011) 960–972.
[76] A. Ostadhossein, E.D. Cubuk, G.A. Tritsaris, E. Kaxiras, S. Zhang, A.C. Van Duin, Stress effects on the initial lithiation of crystalline silicon nanowires: Reactive molecular dynamics simulations using ReaxFF, Phys. Chem. Chem. Phys. 17 (5) (2015) 3832–3840.